Monthly Notices of the ROYAL ASTRONOMICAL SOCIETY

MNRAS **510,** 5348–5361 (2022)
Advance Access publication 2022 January 3

https://doi.org/10.1093/mnras/stab3788

Dynamo activity of the K dwarf KOI-883 from transit photometry mapping

S. M. Zaleski,[1★] A. Valio,[2] B. D. Carter[1] and S. C. Marsden[1]

[1] Centre for Astrophysics, University of Southern Queensland, Toowoomba 4350, Australia

[2] Center for Radio Astronomy and Astrophysics, Mackenzie Presbyterian University, Rua da Consolaçao, SP 01302-907, São Paulo, Brazil

Accepted 2021 December 21. Received 2021 December 20; in original form 2021 May 26

ABSTRACT

The *Kepler* mission target star KOI-883 is notable in being a low-mass K2V dwarf with moderately fast 8.99-d rotation and hosting a single transiting hot Jupiter in a 2.69-d orbit. This combination thus presents a particular opportunity to study star-spot activity by using the many deep planetary transits apparent in the light curve to map the stellar surface. The data have been analysed using spot modelling and temporal mapping methods we have used for other *Kepler* host stars, and a search for flares was conducted. Our results indicate a low-latitude region of the photosphere marked by distinct areas of individual or grouped star-spots with moderately high solar-type differential rotation of 0.102 ± 0.011 rad d^{-1}, but with just two major flares observed across 400 d. These results imply a rotational shear significantly greater than that of our slower rotating Sun. The observed flares are more energetic than typical solar flares, but similar to those of other magnetically active cool dwarfs.

Key words: stars: flare – stars: low-mass – stars: rotation – stars: solar-type – star-spots.

1 INTRODUCTION

Magnetic activity in cool solar-type stars is measured in reference to the activity of the Sun (Reiners 2012). Assuming that a solar-type dynamo is at play in cool stars, the same proxies of magnetic activity may be observed on the Sun and cool stars. Spots in the photosphere are the most prevalent proxy, while flares are another but sometimes less frequent observable. Both spots and flares are associated with active photospheric regions and strong magnetic fields.

Sunspots have long been used as indicators of magnetic activity (Maunder 1904; Hathaway 2015; Covas 2017). Activity in the Sun has its root in magnetic fields generated by the rotation and convection of electrically conducting plasma. The action of an $\alpha\Omega$ dynamo regenerates magnetic fields through the cycling of toroidal fields generated at the base of the convective zone, or tachocline, and poloidal fields created by turbulent helicity (Schrijver & Swaan 2000; Hubbard, Rheinhardt & Brandenburg 2011). Magnetic fields caught in turbulent convective flows are amplified by shearing due to differential rotation and twisted by the Coriolis effect. They then rise and erupt on the photosphere as regions of intense magnetic fields, or sunspots (Hubbard et al. 2011; Isik, Schmidtt & Schussler 2011; Shapiro et al. 2016).

Star-spots are sunspot equivalents prevalent on solar-type stars – those stars having a radiative core encased by a convective envelope. The magnetohydrodynamic processes of a large-scale solar dynamo active in the interiors of solar-type stars trigger the formation of observable star-spots (Berdyugina 2004; Balona & Abedigamba 2016). Generally, the physical attributes of star-spots are expected to differ from sunspots, though their trends may be similar. The physical information gathered from each study of star-spots on cool stars provides new observational constraints of solar dynamo theory and enhances the understanding of solar/stellar magnetic fields. Both sunspots and star-spots are cooler than the quiescent photosphere, though temperature differences relative to stellar effective temperature may differ (Ortiz et al. 2002). Star-spot radial sizes, lifetimes, intensities, temperatures, and locations in latitude and longitude may also vary with spectral type and age. For example, sunspots typically appear at low latitudes, while the appearance of star-spots on cool stars varies from pole to equator (Yadav et al. 2015). Many trends have also been found for stars in the *Kepler* sample. For active solar-type *Kepler* stars, star-spot lifetimes are typically shorter than sunspot lifetimes (see Namekata et al. 2019, and references therein). For FGKM stars, star-spot coverage decreases with decreasing rotation rate following an age–activity relation (Nichols-Fleming & Blackman 2020). Star-spot stability also increases with slowing rotation rates of cool stars (Mehrabi, He & Khosroshahi 2017).

While the physical attributes of star-spots unveil interesting trends, it is the spatial evolution of star-spots on a stellar surface that is fundamental to the measurement of differential rotation caused by the interplay of rotation and convection, an important element of solar dynamo theory. The Sun is known to rotate differentially at 0.073 rad d^{-1} (Beck 2000), with rotation fastest at the equator and slowing with increasing latitude towards the poles. Theory and observation show that solar-type stars cooler than the Sun will have smaller values of differential rotation. Küker & Rüdiger (2005) predicted that for FGK stars differential rotation decreases with decreasing stellar effective temperature. From Doppler imaging (DI) of 10 stars of spectral class G2-M2, Barnes et al. (2005) observed a decrease of surface differential rotation with decreasing stellar effective temperature. In their study of *Kepler* K - A stars, Balona & Abedigamba (2016) also noted similar downward trends in mean rotational shear and mean relative shear as stellar effective temperature decreased with spectral class. The shear of cool, early M dwarfs increases from 0.028 to 0.047 rad d^{-1} as rotation period increases from 1 to 10 d and decreases for

★ E-mail: shelley.zaleski@usq.edu.au

longer rotation periods in response to rotational quenching of the α dynamo effect (Küker et al. 2019). For example, Kepler-45 ($T_{\rm eff}$ = 3820 K, $P_{\rm rot}$ = 15.76 d) is an M1 dwarf and has a differential rotation of 0.031 $\pm$ 0.004 rad d^{-1} (Zaleski et al. 2020). In comparison, the M1 dwarf OT Ser is a rapid rotator ($P_{\rm rot}$ = 3.40 d) with a differential rotation of 0.12 $\pm$ 0.02 rad d^{-1} (Donati et al. 2008).

Photometric, spectroscopic, and spectropolarimetric methods have been employed to construct stellar surface maps from which stellar rotation period and differential rotation may be estimated. DI utilizes broadened spectral line profiles to create 2D surface maps via the correlation of spectral line position to stellar surface position (Vogt & Penrod 1983). Zeeman–Doppler imaging (ZDI) produces both magnetic and temperature distribution maps from polarized radiative Stokes parameters (Semel 1989; Brown et al. 1991; Carroll et al. 2012). Kővári et al. (2017) used Doppler and Zeeman–Doppler mapping to analyse the differential rotation of GKM stars. We refer the reader to Savanov et al. (2018) for a comprehensive discussion on the evaluation of differential rotation.

Applicability of photometric techniques based on the modulation of stellar light curves by star-spots is not limited by stellar rotation rate and magnitude. These techniques include analysis of Lomb–Scargle periodograms (Reinhold, Reiners & Basri 2013; Aigrain et al. 2015) and Lomb–Scargle periodograms combined with autocorrelation of baseline flux (Pan et al. 2020), phase tracking (Davenport, Hebb & Hawley 2015), and autocorrelation of flux deficit due to star-spots (Silva-Valio & Lanza 2011; Valio et al. 2017; Zaleski et al. 2019, 2020; Araújo & Valio 2021). Calculation of flux deficit requires the physical attributes of individual star-spots (radius, intensity, and longitude) occulted during exoplanetary transits whose parameter estimates are obtained via modelling.

Star-spot modelling necessitates visual inspection of all detrended and normalized transit light curves available for a host star. It is also possible to detect out-of-transit mmag amplitude modulations due to flares, which are noticeably larger than those due to spots. Flares are another proxy of magnetic activity generated by a solar-type dynamo and are thought to be associated with active regions (Toriumi et al. 2020). The ambient atmosphere above spots is dominated by flux tubes with intense magnetic fields that contribute to flare emission (Gordovskyy & Lozitsky 2014). Magnetic reconnection of antiparallel field lines, such as those for spot pairs, changes magnetic topology and triggers the conversion of stored magnetic energy to thermal and kinetic energy with subsequent emission of broad spectrum radiation (Joshi et al. 2012). Solar flares release 10^{28}–10^{32} erg for flare durations of minutes to hours (Shibata & Megara 2011). The largest solar flare recorded is the Carrington flare of 1859 with an estimated energy of 10^{32} erg (Carrington 1859).

Spotted solar-type stars are all candidates for flaring events. Flare rates vary among spectral types while also following an age–activity relation (Davenport 2016; Ilin et al. 2019). Star-spot coverage of the stellar surface and flare frequency both decrease with increasing stellar rotation period, indicative of lessening magnetic activity. The relation between stellar mass and flare activity is not as clear, though study suggests an increase in flaring with decreasing mass for GKM field dwarfs in the *Kepler* sample (Davenport et al. 2019). The lower masses of K and M cool dwarfs enhance the observability of flares in 'white light' due to their contrast with the luminosity of the quiet photosphere (Jackman et al. 2021). Ilin et al. (2019) extracted 751 stars in a sample of 1761 stars (largely late-K to mid-M dwarfs) from the K2 mission having flares with energies of the order of 10^{32}–10^{34} erg. In a search for flares in over 20 000 stars from the first *TESS* data release for sectors 1 and 2, approximately 1100 flaring stars were found of which more than half were M dwarfs with flare energies similar to those for M dwarfs observed by the K2 mission (Günther et al. 2020).

In this work, we present our analysis of the activity of the faint orange dwarf KOI-883 from the modelling and mapping of star-spots in transit light curves recorded by the *Kepler* mission. System parameters and observational data are presented in Section 2. The transit model is described in Section 3. Star-spot parameters, temporal mapping of star-spots, and magnetic activity (differential rotation, short cycles, and flares) are discussed in Section 4. We conclude with a summary and discussion in Section 5.

2 KOI-883 SYSTEM PARAMETERS AND OBSERVATIONS

2.1 A faint orange dwarf

From the launch of the primary mission on 2009 March 7 to the end of data collection on 2013 May 11, the *Kepler* telescope recorded data for more than 150 000 stars in the Cygnus–Lyrae region. While originally intended to search for Earth-size exoplanets transiting in the habitable zones of stars (Borucki 2010), a wealth of stellar information is contained in light curves collected at two cadences, a long cadence (LC) of 29.4 min and a short cadence (SC) of 58.85 s. Light curves of many stars modulate sinusoidally with amplitude changing according to the degree of spottedness, or magnetic activity, as star-spots emanate and erode in the photosphere while the star rotates (Mehrabi et al. 2017).

Initially observed during the first 16 months of the *Kepler* mission, KOI-883 (or K00883.01, KIC 7380537, 2MASS J19464393+4258043) is a K dwarf orbited by a single hot Jupiter (Batalha et al. 2013). LC light curves are available for all 17 *Kepler* quarters, covering the period from 2009 May 13 to 2013 May 11. SC light curves were recorded during quarter 10 (2011 June 26 to 2011 September 28) and quarters 13 through 17 (2012 March 29 to 2013 May 11). The sinusoidal modulations in both LC and SC light curves evidence changes in total irradiance due to star-spots, or magnetic activity, as shown by the SC light curves in Fig. 1.

KOI-883 is an orange dwarf known to be transited by a hot Jupiter. Other K dwarfs orbited by a Jupiter-sized exoplanet include WASP-52 (Hebrard et al. 2013), WASP-59 (Hebrard et al. 2013), WASP-67 (Hellier et al. 2012), Qatar-1 (Alsubai et al. 2011), and Qatar-2 (Bryan et al. 2012). Analyses of these five star–planet systems focused largely on stellar and planetary physical parameters from spectroscopic and/or photometric observations. Mancini et al. (2014) investigated the physical parameters of both the star and planet in the Qatar-2 system and measured the planet's orbital obliquity via star-spot tracking. A later study of Qatar-2 by Dai et al. (2016) addressed star-spot crossing for the measurement of stellar obliquity. Mancini et al. (2017) also used repeated star-spot crossings to estimate the projected and true orbital obliquities of WASP-52b. Our examination of KOI-883 is the first to retrieve a short magnetic cycle and stellar differential rotation from individual star-spots.

KOI-883 is a faint solar-type star. It is smaller and less massive than the Sun at 0.70 $R_\odot$ and 0.69 $M_\odot$ (refer to Table 1 for a summary of stellar parameters). Batalha et al. (2013) first estimated a stellar radius of 0.58 $R_\odot$ from the early *Kepler* data. Since then, parallaxes and distances from the *Gaia* mission have improved the stellar radius measurements of stars previously observed by *Kepler*. Szabo et al. (2013) classified KOI-883 as an early K dwarf from Kepler Input Catalog parameters. *Gaia* Early Data Release 3 provides the most recent estimate of $T_{\rm eff} = 4840^{+140}_{-190}$ K. The correspondence between spectral type and $T_{\rm eff}$ places KOI-883 in stellar class K2V at the

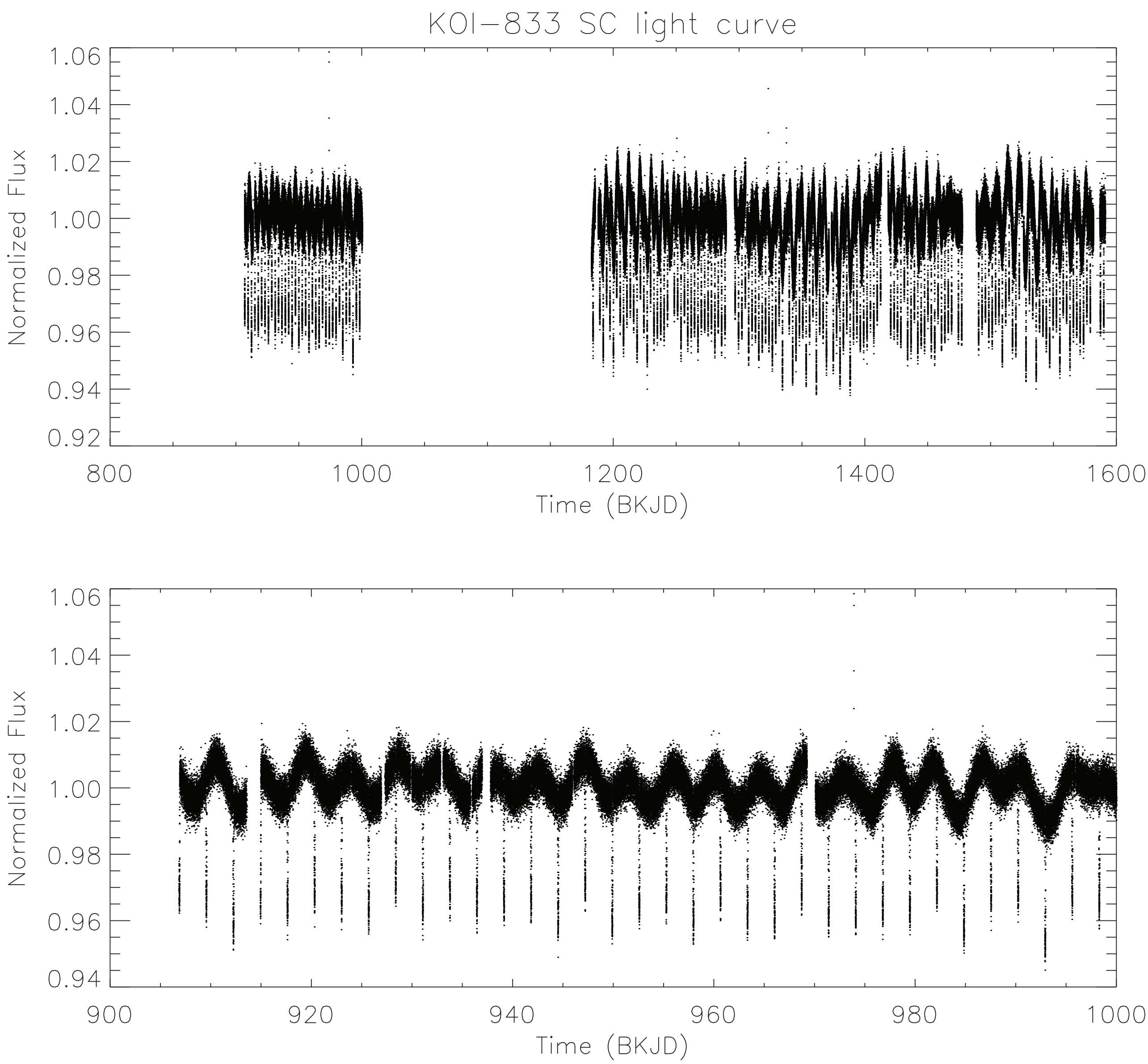

Figure 1. Top: SC light curves of KOI-883. Bottom: Extract of the first 100 d of light-curve data with a flare at 973.9 d.

median value of $T_{\rm eff}$, with an uncertainty of one step in class, i.e. K1V–K3V. Szabo et al. (2013) also estimated a rotation period of 9.1 d from Fourier analysis of light curves from the first 6 *Kepler* quarters. 2 yr later, Holczer et al. (2015) estimated a stellar rotation period of 9.02 d. We have refined that value to 8.994 d (see Section 4).

An approximation of the age of KOI-883 can be inferred from the distributions of rotation period and stellar age versus the difference between mean photometric magnitudes in the *Gaia* blue and red passbands, $G_{\rm BP}$ and $G_{\rm RP}$, generated for a pseudo-sample of *Kepler* stars via the gyrochronology/rotation period model of Angus et al. (2019). The distributions follow the Praesepe-calibrated gyrochronology for late F, G, K, and early M dwarfs. For the *Gaia* magnitude difference $G_{\rm BP} - G_{\rm RP} = 1.336$, $G_{\rm BP} = 16.370$ and $G_{\rm RP} = 15.034$ (Gaia Collaboration 2016, 2021; Riello et al. 2021), or a stellar rotation period of 9 d, the age of KOI-883 falls just below the 1 Gyr Praesepe-calibrated line. The estimated age of KOI-883 does not consider variations in stellar rotation period due to tidal interactions with its exoplanet and shortcomings in gyrochronological relations (Brown 2014); however, we suggest that the estimate is suitable to the purposes of this work.

2.2 A transiting hot Jupiter

KOI-883's transiting hot Jupiter, which we refer to as KOI-883b, completes its orbit every 2.69 d along a projected stellar latitude of -24.99°. A list of KOI-883b parameters is given in Table 1. All KOI-883 transit light curves are publicly available at MAST (Mikulski Archive for Space Telescopes).[1] While LC light curves serve for determination of the mean stellar rotation period, the temporal precision of deep transits recorded in SC mode is needed for the identification of small amplitude modulations due to individual star-spots or star-spot groups in the stellar photosphere occulted by the planet during its transit. During transits, star-spots are discernible

[1] http://archive.stsci.edu/kepler/

Table 1. Star-exoplanet parameters of the KOI-883 system.

Parameter	Value	Ref
Star		
Spectral type	K2V	1
Kepler magnitude (K_p)	15.766	2
Mass ($M_\odot$)	$0.70^{+0.06}_{-0.07}$	2
Radius ($R_\odot$)	$0.69^{+0.07}_{-0.04}$	3, 4, 5
Effective temp (K)	4840^{+140}_{-190}	3, 4, 5
Rotation period (d)	8.994 ± 0.016	1
Age (Gyr)	~ 1	1
Limb darkening coeff, c_1	0.465 ± 0.018	6
Limb darkening coeff, c_2	-0.269 ± 0.040	6
Limb darkening coeff, c_3	0.987 ± 0.039	6
Limb darkening coeff, c_4	-0.420 ± 0.014	6
Planet		
Mass ($M_{♃}$)	n/a	
Radius ($R_{♃}$)	$1.265^{+0.017}_{-0.018}$	1
Radius ($R_\star$)	$0.1835^{+0.0029}_{-0.0037}$	1
Semimajor axis (au)	$0.03495^{+0.00094}_{-0.00119}$	1
Semimajor axis ($R_\star$)	$10.84^{+0.29}_{-0.37}$	1
Inclination angle (°)	$92.23^{+0.37}_{-0.23}$	1
Orbital period (d)	2.688899^{+8e-6}_{-9e-6}	2
Orbital obliquity (°)	≤ 4	7

Note. 1: This work, 2: Kepler Objects of Interest Cumulative Table, DOI:10.26133NEA4, accessed 2020 December 15, 3: Gaia Collaboration (2016), 4: Gaia Collaboration (2021), 5: Riello et al. (2021), 6: Bourque et al. (2021), 7: Dai et al. (2018).

as bumps, or flux increases, whose durations are of the order of minutes. We visually inspect each transit from the detrended Pre-search Data Conditioning Simple Aperture Photometry (PDCSAP) SC light curves from *Kepler* Data Release 25 (Thompson et al. 2016a). Instrumental noise and non-astrophysical effects have been removed from PDCSAP light curve by the SOC 9.3 pipeline, leaving star-spot signatures unaffected (Jenkins et al. 2010; Smith et al. 2012; Stumpe et al. 2012). To further ensure that the data do not contain artefacts due to spacecraft events or pipeline flagged phenomena, only data having a zero quality flag are extracted from the LC and SC FITS files (Thompson et al. 2016b).

The latitude of all star-spots is the transit latitude, determined by the semimajor axis of the hot Jupiter's orbit and the inclination of the orbital plane with respect to the stellar rotation. By applying our transit model (Silva 2003) in a Bayesian framework, we derive their physical characteristics such as radial size, intensity, and longitude (see Section 3). The centre time of the 'bump' due to a star-spot is first converted to longitude in the observer's frame and then to stellar topocentric longitude. Star-spot parameters are used to construct a temporal map of the stellar surface from which rotation period at the transit latitude may be estimated. Using the mean stellar rotation period calculated from LC data and assuming a solar-like differential rotation profile, the differential rotation of KOI-883 may be estimated and assessed relative to differential rotation values for FGKM dwarfs. This methodology has been previously employed to measure stellar rotation for several *Kepler* solar-type stars: Kepler-17 (Valio et al. 2017), Kepler-63 (Netto & Valio 2020), Kepler-71 (Zaleski et al. 2019), Kepler-45 (Zaleski et al. 2020), and Kepler-411 (Araújo & Valio 2021).

Given that KOI-883 is an early orange dwarf with a mean $T_{\rm eff}$ of 4840 K, we expect to find a differential rotation value in the range 0.03–0.11 rad d^{-1} calculated by Reinhold et al. (2013) for *Kepler* stars with $T_{\rm eff}$ from 3500 to 6000 K. The differential rotation of young stars increases as stellar temperature increases (Barnes et al. 2005; Balona & Abedigamba 2016). We also expect to profile solar-type differential rotation, as proposed by Matt et al. (2011) from their simulations of differential rotation in K stars having masses of 0.7 and 0.9 $M_\odot$.

3 THE MODEL

We apply our transit model *eclipse*[2] (Silva 2003) in a Bayesian framework to all candidate star-spots noted in SC light curves to derive a priori values of star-spots physical properties (radial size, intensity, and longitude). The model simulates the path of a planet represented as a dark, solid disc as it crosses a 2D white light image of the star. This star may have either spots or faculae on its surface which are modelled as circular features of a certain radius and intensity on the 2D star image (see top panel of Fig. 2). The effect of foreshortening is taken into account when these features are close to the limb. Each spot is represented by three parameters: radius, intensity, and longitude. The latitude of the spot centre is assumed to be that of the centre of the planet transit chord. The trajectory of the planet in its orbit (which can be eccentric) is simulated, with a precision of 1 min, and the addition of the pixels intensity of the 2D image of star (with or without spots) plus planet (with rings and/or moons) results in the transit light curve brightness at that time interval.

The stellar image is limb darkened following the four parameter limb darkening law for its ability to precisely represent centre-to-limb variations Claret (2000), Sing (2010), Claret & Bloemen (2011), Claret, Hauschildt & Witte (2012), and Neilson et al. (2017).

$$\frac{I(\mu)}{I(1)} = 1 - c_1(1-\mu^{1/2}) - c_2(1-\mu) - c_3(1-\mu^{3/2}) - c_4(1-\mu^2), \quad (1)$$

where $I(1)$ is the maximum intensity at disc centre and $\mu = \cos(\theta)$, where θ is the angle between the line of sight and the surface normal $\hat{n}$. The limb darkening coefficients c_1, c_2, c_3, and c_4 generated using the Phoenix ACES model are available from the ExoPlanet Characterization Toolkit.[3]

The planet's orbit is assumed to be circular and coplanar with the stellar equator. Neither the orbital eccentricity nor the angle of periastron has been constrained via RV measurements. Dai et al. (2018) estimated the obliquity of KOI-883 to be less than 4°. The orbits of hot Jupiters orbiting low-mass stars below the Kraft break ($T_{\rm eff}$ = 6200 K) are well aligned with the stellar spin axis due to strong magnetic braking and tidal interaction (Kraft 1967; Eggleton & Kiseleva-Eggleton 2001; Winn et al. 2010; Dawson 2014; Becker et al. 2017). Albrecht et al. (2012) observed this trend in their study of the obliquities of 14 hot Jupiter-hosting stars. Tregloan-Reed et al. (2015) also found that the WASP-6 system ($T_{\rm eff}$ = 5375 K) is well aligned at a sky projected angle of $7° \pm 4°$. Strong tidal interactions may also act to circularize the short-period orbits of hot Jupiters on shorter time-scales as compared to cooler giant planets in orbits with non-zero eccentricities (Hamer & Schlaufman 2019). As such, we assume a circular orbit for KOI-883b and a planet–star distance at mid-transit that does not vary.

The planet's position is calculated in steps of 1 min spanning ± 4 h about mid-transit, or t = 0 h. For steps at which the planet's disc overlays the stellar image, the total stellar intensity is reduced by the total intensity of the planet's obscured stellar area. This

[2] https://github.com/biaduque/astronomy.
[3] https://exoctk.stsci.edu/limb_darkening

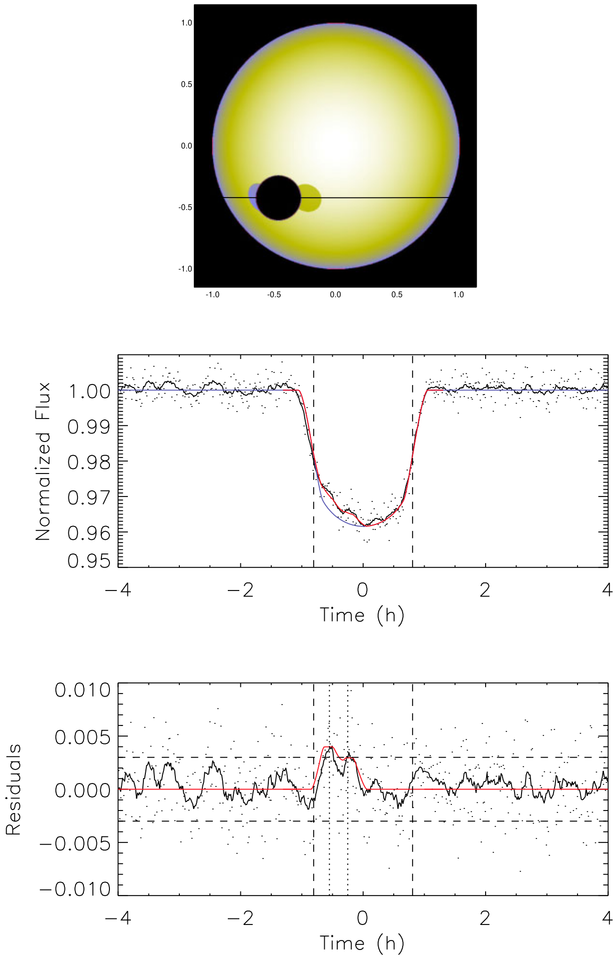

Figure 2. The simulated star with two spots and the transiting planet depicted by a black disk (top). Transit 19 observed data after 10 point smoothing is shown in black with an overlay of the unspotted model in blue and a model with two spots in red (middle). Mid-transit time ($t = 0$ h) at 0° stellar longitude in the observer's frame corresponds to 960.6385 BKJD. The residuals (black) represent the subtraction of the model from data (bottom). The horizontal dashed lines represent ±5 times the rms of a spot-free transit. The red line is the two spot model after a spotless star model subtracted. The dotted vertical lines cross star-spots at −0.25 h and −0.55 h, corresponding to stellar longitudes of −15.25° and −41.8°, respectively. The dashed vertical lines mark ± 70° stellar longitude.

procedure generates a smooth transit light curve model extending beyond ingress and egress of the planet.

In conjunction with the stellar radius and limb darkening law, the planetary radius, orbital semimajor axis, and inclination contribute to the overall shape of the planetary transit. To obtain the optimal transit model, published values of the planetary parameters are refined by fitting them to an average of 161 complete and unbroken SC transits after normalization and phase folding. Averaging removes star-spot signatures that can effect transit depth. Fitting is performed via an Interactive Data Language (IDL) version of the Goodman & Weare (2010) Markov chain Monte Carlo (MCMC) ensemble sampler first implemented in PYTHON by Foreman-Mackey et al. (2013). The algorithm draws samples from a posterior probability distribution consistent with system parameters. Uniform priors for the planet's radius, orbital semimajor axis, and inclination are given in Table 2.

Table 2. Uniform priors for model light-curve fitting.

Parameter	Range
Planet radius ($R_\star$)	[0.1–0.2]
Semimajor axis ($R_\star$)	[9–16]
Inclination angle (°)	[80–100]

Table 3. Secondary transit parameters.

Parameter	Value
Transit latitude (°)	$-24.99^{+5.4}_{-3.6}$
Impact parameter	$-0.42^{+0.06}_{-0.08}$
Transit duration (h)	2.12 ± 0.04

Transit duration is the difference between the times of ingress and egress in the model. The impact parameter, b, and transit latitude, lat_{tran}, are derivatives of the planet's orbital inclination and semimajor axis. For circular orbits, they are given by

$$b = \frac{a\cos(i)}{R_\star} \tag{2}$$

$$lat_{\mathrm{tran}} = \arcsin\left(\frac{a}{R_\star\cos(i)}\right), \tag{3}$$

where a is the semimajor axis, $R_\star$ is the stellar radius, and i is the inclination of the planet's orbit.

Values of these secondary parameters are listed in Table 3. The sign of the transit latitude projection cannot be determined. We have chosen transits to occur across the star's Southern hemisphere.

Thus far, we have established a parameter set for the hot Jupiter transiting the unspotted surface of KOI-883. The next, and major, step is studying magnetic features on the stellar photosphere by comparing the transit model to each transit extracted from the SC light curves. While the transit model is a smooth curve, true light curves are inherently irregular. Though the data have been detrended and pre-conditioned, inherent noise due to stellar variability remains. Subtraction of the model from data will yield irregular residuals, and it is the amplitudes of the irregularities that distinguish noise from star-spots. The rms of out-of-transit data will be less than that of in-transit data when star-spots are occulted by the planet. The rms values for KOI-883 are 0.00320 in-transit and 0.00296 out-of-transit when considering all unbroken transits. Therefore, there is an increase of 8 per cent in the noise within transits due to star-spots.

The selection of individual star-spots for analysis is based on the in-transit rms of spot-free transits. Upon visual examination, a subset of transits having low noise residuals and no signatures of star-spots and/or faculae were extracted from all unbroken transits. The 1σ in-transit rms of those spot-free transits is 0.00059. When examining the residuals between the transit model of a spotless star and each observed light curve, we require that inferred flux modulations due to star-spots have residuals of no less than 5σ, or 5 times the in-transit rms of a spot-free transit. The time at the peak of a qualifying residual, i.e. the time at maximum amplitude variation due to a star-spot, corresponds to the centre longitude of a star-spot. A series of peaks relatively close in time may indicate a star-spot group.

The upper panel of Fig. 2 depicts the 19th transit of KOI-883b across a simulated spotted stellar face. The irregular black curve in the middle panel represents observed data smoothed every 10 points. Mid-transit time (t = 0 h) corresponds to 960.6385 BKJD (Barycentric Kepler Julian Date defined as Barycentric Julian Day minus an offset of 2454833 corresponding to 12:00 on 2009 January 1 UTC). The u-shaped blue curve is the unspotted transit model. The reduction in normalized flux from approximately −0.50 h to −0.25 h signals the occultation of a star-spot group. The red curve is a 2-spot transit model fit to observed data. The lower panel of Fig. 2 pictures the residuals remaining after the subtraction of the unspotted model (black) and spotted (red) models from observed data. The peaks at −0.25 h and −0.50 h above 5σ, or 5 times the in-transit rms of a spot-free transit (dashed horizontal line) are interpreted as 2 star-spots, indicated by the vertical blue dotted lines in Fig. 2.

A star-spot is defined by its radius, intensity, and longitudinal position along the transit chord. Star-spot latitude is not included as a variable parameter and is assigned the transit latitude of −24.99° though the transit band covers 32° of the star's surface due to the exoplanet's radial size. Star-spots radius and intensity are inferred by the width and amplitude of the bump-shaped modulations. The central longitude is estimated by converting residual peak time to the projected longitude of the planet's crossing, given as

$$lon_s = \arcsin\left[\frac{a\cos\left(90^\circ - \frac{360^\circ}{24}\frac{t_s}{P_{\rm orb}}\right)}{\cos(lat_{\rm tran})}\right], \tag{4}$$

where a is the semimajor axis in units of stellar radius, $P_{\rm orb}$ is the orbital period, $lat_{\rm tran}$ is the transit latitude, and t_s is the residual peak time.

A longitude of 0° corresponds to mid-transit, or $t = 0$ h. Only star-spots with longitudes within ±70° are considered in order to avoid the walls of a transit well (Silva-Valio et al. 2010). Hence, the residual peaks at ±70° are transit wall effects and are not considered.

Each spotted transit detected in the set of SC light curves is fit to a unique transit model with star-spots. The number of star-spots added varies among transits. While most star-spots are seen as distinct bumps in observed data, long temporal variations with residual peaks close in time infer a star-spot group. We find that two or three star-spots are sufficient representation of a group. In general, no more than four model star-spots are needed to simulate each transit observation.

Our model with added spots serves as the generative model which MCMC employs to fit a spotted model to observed data by simultaneously optimizing the free parameters of radius, intensity, and longitude within the ensemble space delimited by flat priors. Star-spot radius is defined in units of planetary radius R_p, with uniform priors [0.2, 2.0]. Intensity is constrained from 0 to less than 0.9 the surrounding photosphere intensity to ensure values above the *Kepler* noise floor. The model considers the limb darkened stellar face and as such incorporates limb darkening into the intensity of star-spots relative to their longitudes. Longitude is the converted residual peak time from equation (4) and must be within the range [−70, 70] deg. Since the MCMC sampler begins its walks through ensemble space from initial parameter values, we set 0.5 R_p and 0.5 I_c as the initial guesses for star-spot radius and intensity. A large number of walkers are required for the sampler to forget where it began. This demands running long chains that may draw as many as 10^6 samples from the probability distribution. Parameter median values and 1σ uncertainties are discussed in the following section.

4 RESULTS

4.1 Star-spot radii and longitudes

KOI-883 is expected to be magnetically active in view of its age and moderately rapid rotation period. Consequently, star-spots may be occulted during the passage of a sizeable planet with a radius of 1.265 $R_{♃}$ over a significant and potentially active area of its host surface. The 92.2° inclination of KOI-883b's orbit relative to the stellar rotation axis ensures near maximum coverage at lower latitudes (Tregloan-Reed & Unda-Sanzana 2021). If star-spots on KOI-883 are present at mid- to low-latitudes as they are on the Sun, the probability of their detection is favourable since the transit band is approximately within −9° and −41° latitudes due to the size of the planet.

The short orbital period of the transiting hot Jupiter KOI-883b benefits the observer by having allowed hundreds of deep transits to be recorded during the *Kepler* mission. The added precision of SC data and the mean transit depth of 3.8 per cent for a large planet orbiting a small star provide the sensitivity critical to finding star-spots with relative amplitudes below 0.5 per cent. We found 49 transits with a total of 78 star-spots that met or exceeded the out-of-transit rms threshold. All star-spots were modelled as described in the previous section. Additional favourable parameters that allow for star-spot detection, such as data precision, data cadence, observed wavelength, and large k to name a few. To verify that the addition of star-spots to an unspotted model yields a spotted model that better fits observed data, the Bayesian Information Criterion (BIC) was employed to assess the quality of spotted models. Assuming that the model errors are independent and that the model parameters have been well constrained by the MCMC algorithm, the BIC may be redefined in terms of the error variance as (Clement 2014)

$$BIC = n\ln(\sigma^2) + k\ln(n), \tag{5}$$

where σ^2 is the error variance, or in the alternate form,

$$BIC = \chi^2 + k\ln(n), \tag{6}$$

where χ^2 is the goodness-of-fit of a model to observed data, n is the number of data points, and k is the penalty factor.

When the number of free parameters differs between models, the penalty term $k\ln(n)$ aids in resolving the difference between models. While a more complex model is expected to trend well to the data and yield a lower metric than a simpler model, that model is penalized for extra parameters when computing the metric. Each star-spot carried a penalty of 3 corresponding to the statistical parameters of radius, intensity, and longitude.

For the 49 transits having from one to four spots, the mean score for over 700 observed data points compared to an unspotted transit model was 205.78. A lower mean score of 194.58 was calculated when observed data was compared to a spotted transit model. Subtraction of the unspotted score from the spotted score yields a difference of −11.20, an indicator of the better quality of star-spot-added transit light-curve models.

Histograms of the maximum a priori radii and longitudes are given in Fig. 3. The mean radius of fit star-spots is 0.65 ± 0.29 R_p, or 11° ± 5°, or (5.7 ± 2.6) × 10^4 km. Star-spot minimum and maximum radii are 0.11 and 1.37 R_p, or 1.8° and 22.6°, or 9.7 × 10^3 km and 1.21 × 10^5 km, respectively. The largest star-spots have radii greater than that of the largest sunspot observed at solar maximum, or 5 × 10^4 km (Morris et al. 2017). Star-spots whose radial measure is much greater than that of large sunspots have been detected on other main-sequence stars. For example, star-spots on CoRoT-2 are 10 times the size of a large sunspot (Silva-Valio et al. 2010), and the largest occulted active regions on Kepler-17 are 3–4 times the size of the largest sunspot groups (Bonomo & Lanza 2012).

Since star-spots are being evaluated against a noisy photometric background, it is not surprising to observe less small spots than large spots (Solanki 2002). Due to the noise in the light curves precluding the division of a star-spot group into smaller components, the large spot radii may indicate groups of smaller star-spots or sunspot-sized spots (Solanki 2002), but it is not possible to make this distinction with the data at hand.

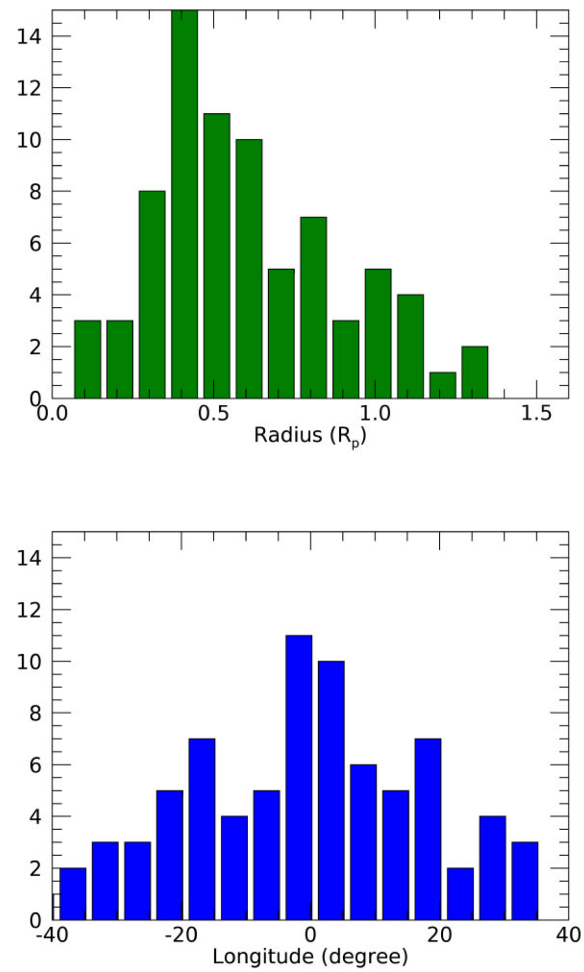

Figure 3. Histograms of star-spot radii (top) and longitudes (bottom) in the reference frame of the observer. One planet radius, R_p, is equivalent to 16° of the stellar hemisphere.

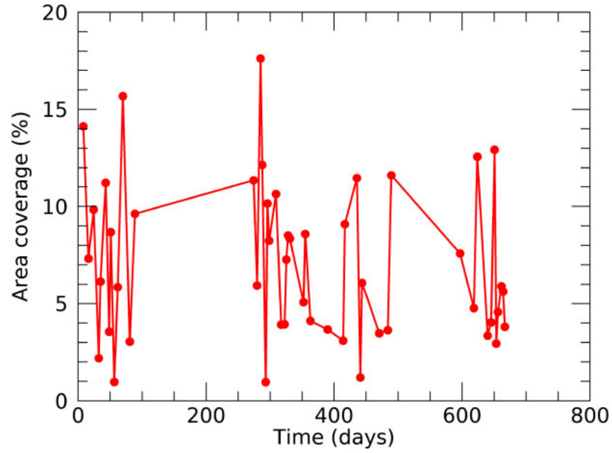

Figure 4. Occulted stellar surface area covered by spots in time. The average star-spot coverage within the transit band is 8 ± 4 per cent.

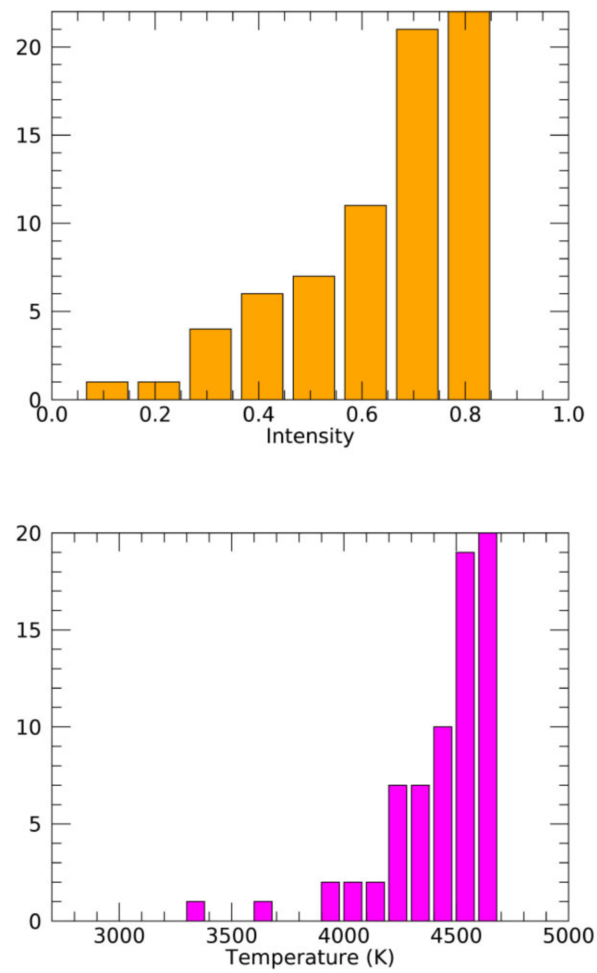

Figure 5. Histograms of star-spot intensities (top) and their respective temperatures (bottom) as estimated via equation (7).

Each transit was visually inspected for star-spots at longitudes within ± 70° relative to 0° in the frame of the observer to avoid stellar limb effects. In agreement with a hot flux tube model of sunspots (Schüssler et al. 1996; Li, Sofia & Belvedere 2005), we found that the star-spots on KOI-883 are discernible at longitudes close to the central meridian. Neither the observed transits nor the residuals resulting from the subtraction of a spotless transit model from those transits suggested star-spots at longitudes greater than 40° or less than −40°. As can be seen in the histogram in the bottom panel of Fig. 3, star-spot longitudes span approximately ± 40° from the centre of the stellar face.

The star-spot area coverage was estimated considering the derived star-spot radii and the total stellar area occulted by the planet during its transit. The results are plotted in Fig. 4, and the average stellar surface covered by spots at a given time is 7 ± 4 per cent within the transit band.

4.2 Star-spot intensities and temperatures

We determine the mean star-spot intensity to be $0.70 \pm 0.17\, I_c$, where $I_c(\mu = 1)$ is the central intensity of the photosphere. The minimum and maximum star-spot intensities are 0.11 and 0.88 I_c, as shown in the top panel of Fig. 5. The ratio between the star-spot and photosphere intensities indicates the degree to which convective flow is suppressed by magnetic fields in active regions (Biazzo et al. 2006). The smaller the intensity value, the darker and cooler the spot with increasing magnetic field strength. Star-spot temperature contrast to the photosphere tends to decrease as stellar effective temperature decreases. Star-spot temperatures are 2000 K less than the surrounding photosphere for the warmest G stars and of the order of a few hundred degrees less than the surrounding photosphere for cool M stars (Berdyugina 2005; Afram & Berdyugina 2015).

Assuming that the star and star-spots radiate as blackbodies, star-spot intensity is converted to temperature via *Planck*'s Radiation Law as expressed by the ratio of star-spot to photosphere intensities given by Silva (2003).

$$\frac{I_{\rm spot}}{I_{\rm phot}} = \frac{\exp\left(\frac{hc}{\lambda K_{\rm B} T_{\rm eff}}\right) - 1}{\exp\left(\frac{hc}{\lambda K_{\rm B} T_{\rm spot}}\right) - 1}, \tag{7}$$

where h is *Planck*'s constant, c is the speed of light, $K_{\rm B}$ is Boltzmann's constant, λ is the *Kepler*-band optimal response wavelength of 600 nm, and $T_{\rm eff}$ and $T_{\rm spot}$ are the photosphere and star-spot temperatures, respectively. For $I_{\rm phot} = 1$, the left-hand side of equation (7) is simply $I_{\rm spot}$. While the bandpass of the *Kepler* photometer is 430–890 nm full width at half-maximum (FWHM), we consider only the optimal response wavelength, which approximates the mean wavelength for observations of solar-type stars (see Gilliland et al. 2011, and references therein).

We find the mean spot temperature to be roughly 350 K lower than the stellar effective temperature (= 4840 K). The average spot temperature is 4500 ± 250 K. As shown by the histogram in the bottom panel of Fig. 5, the minimum and maximum star-spot temperatures are 3340 and 4715 K, respectively, but only 2 star-spots have a temperature of less than 3700 K. Considering the star-spots with temperatures between 3956 and 4715 K, the contrasts cover a broad range from approximately 880 to 110 K. The star-spot-photosphere contrasts measured for other K dwarfs having effective stellar temperatures close to KOI-883, such as IM Peg, II Peg, IN Vir, and VY Ari, range from 900 to 1200 K (see Anderson & Korhonen 2015, and references therein).

4.3 Activity cycles

The Sun exhibits activity cycles of varying lengths, short-term cycles such as the 154-d periodicity and 1 to 3 yr quasi-biennial oscillations, and long-term cycles such as the Schwabe and Gleissberg cycles (Hathaway 2015; Oláh et al. 2016; Deng et al. 2019). Long-term cycles represent the global magnetic activity of the solar dynamo of the order of the 11-yr cycle, while short-term cycles reflect dynamo processes at the tachocline and the quasi-periodic appearance of spots in localized active regions (Deng et al. 2019). Just as the variation in sunspot number, location, and area disclose the Sun's many cycles, star-spot variations are fundamental to determining cycles on solar-type stars.

Short period K dwarf stars are expected to display a high level of magnetic activity (Bondar, Katsova & Livshits 2019). Very young, ultra-fast dwarf stars display a high level of saturation, particularly in chromospheric emission (Jeffries et al. 2011). As dwarf stars evolve and their rotation slows due to the loss of angular momentum, internal processes switch to those of a solar dynamo. Organized solar-type activity cycles appear at a transitional rotation period of approximately 3.3 d for K dwarfs (Nizamov, Katsova & Livshits 2017; Bondar, Katsova & Livshits 2019). Oláh et al. (2016), Suarez Macareno, Rebolo & Gonzalez Hernandez (2018), Bondar et al. (2019) have found photometric cycles of FGKM stars ranging from 2 to 14 yr from decades of observations. See et al. (2016) found similar results from ZDI mapping.

For stellar observations taken on shorter time-scales than decades, such as the almost 4 yr of the *Kepler* mission, short-term stellar activity may be estimated from the star-spots occulted during transit

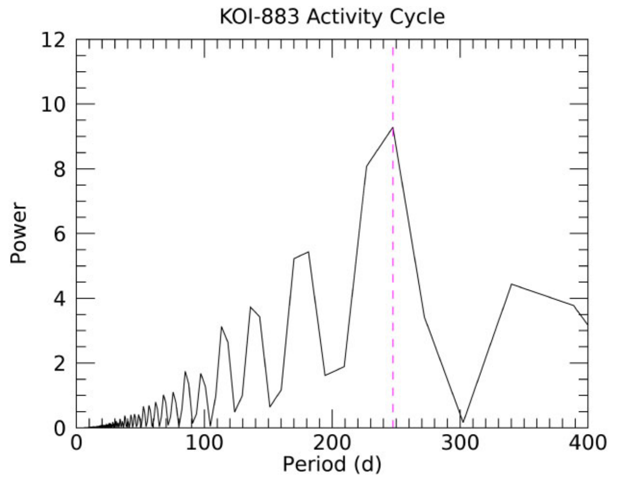

Figure 6. Lomb–Scargle period of flux deficit due to star-spots. The vertical line intersects the curve at peak power, corresponding to a short activity cycle of 247 d.

Table 4. Short-term cycles of *Kepler* GKM stars.

Star	$P_{\rm cyc}$ (d)	$P_{\rm rot}$ (d)	$P_{\rm cyc}/P_{\rm rot}$	$1/P_{\rm rot}$	Ref
KOI-883 (K2V)	247 ± 26	8.994	27.5	0.111	1
Kepler-45 (M1V)	295 ± 50	15.8	18.7	0.063	2
Kepler-3 (K4V)	305 ± 60	30	10.2	0.033	3
Kepler-17 (G2V)	410 ± 50	11.9	34.5	0.084	3
Kepler-63 (G2V)	460 ± 60	5.4	85.2	0.185	3

Note. 1: This work, 2: Zaleski et al. (2020), 3: Estrela & Valio (2016).

via calculation of a Fourier-like power spectrum of flux deficit (Estrela & Valio 2016; Zaleski et al. 2020). Star-spot physical characteristics can be converted into flux deficits that vary per transit with stellar magnetic activity. The flux deficit of individual star-spots is defined as the product of intensity difference from the central photosphere and star-spot area. Thus, the total flux deficit per transit is defined by

$$F_{\rm def} = \sum (R_{\rm spot}/R_\star)^2 (1 - I_{\rm spot}), \tag{8}$$

where $F_{\rm def}$ is the total flux deficit per transit due to spots, $R_{\rm spot}$ and $R_\star$ are the spot and stellar radii, and $I_{\rm spot}$ is spot intensity.

A Lomb–Scargle periodogram of the temporal flux deficit for KOI-883 reveals a short-term activity cycle of 247 ± 26 d, as depicted by the prominent peak in Fig. 6. For comparison, the known short activity cycle lengths and rotation periods for *Kepler* GKM stars are listed in Table 4. Magnetic activity and cycle length, or cycle period $P_{\rm cyc}$, are both dependent on rotation rate. The faster the rate of stellar rotation, the greater the activity and the shorter the cycles. The plot in Fig. 7 shows a positive correlation between ($P_{\rm cyc}/P_{\rm rot}$) versus ($1/P_{\rm rot}$). The short cycle lengths for the *Kepler* dwarf stars in Table 4 increase with decreasing stellar rotation period. This trend is reminiscent of similar plots for long cycles of the order of years (Oláh et al. 2016; Bondar et al. 2019). Here, the trend focuses on a cycle period to rotational period space where the ratio is between 10 and 100. Ratio values for long cycles are generally above 100.

4.4 Flares

Active stars on the main sequence are known to release explosive bursts of energy, or flares (Pettersen 1989). Flares result from the re-connection of magnetic loops in active regions generated via dynamo

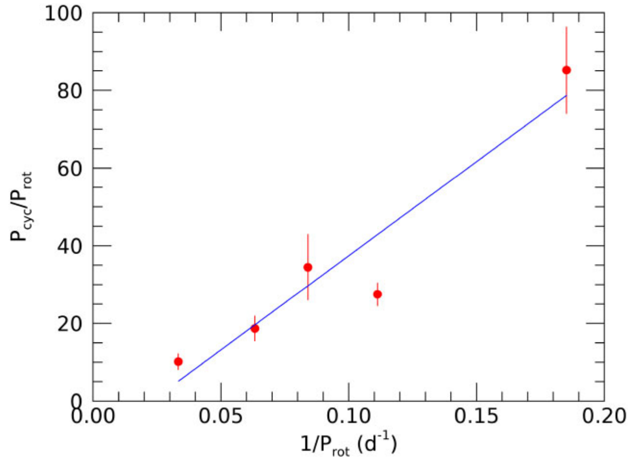

Figure 7. Short cycle length versus inverse stellar rotation period. Known short cycle lengths for *Kepler* dwarf stars increase as rotation period decreases.

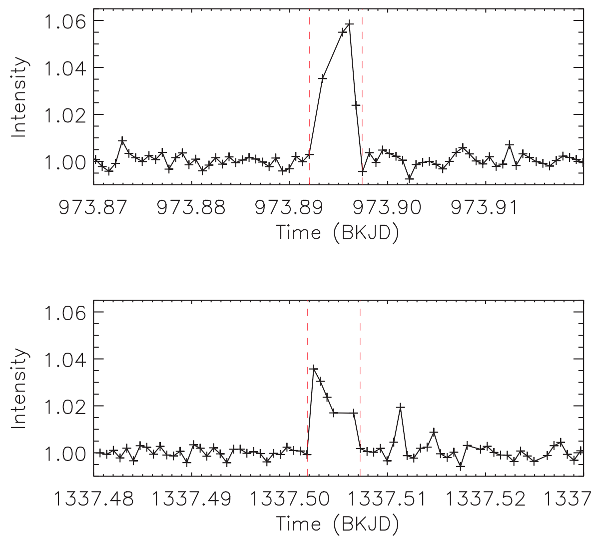

Figure 8. Two superflares from KOI-883 detected with peak intensity of normalized flux at 973.8961 (top panel) and 1337.5025 BKJD (bottom panel). The vertical dashed lines delimit flare duration. Flare energies are of the order of 10^{34} erg.

processes in solar-type stars. Radiated energy is observed across the magnetic spectrum, including X-ray, optical, and radio wavelengths. Flare energy increases with stellar radius and luminosity (Balona 2015). Differential rotation and its interaction with the rotational motion of star-spot pairs and groups in active regions is believed to affect flare energy, though the mechanism remains an open issue (Yan, Wang & Kong 2008; Grimes, Pinter & Morgan 2020).

The flaring activity of cool dwarfs increases from spectral type F to spectral type M. The most recent flare catalogue of stars from *Kepler* LC photometry indicates that M dwarfs have the highest incidence of flaring, followed by K dwarfs (Yang & Liu 2019). M and K dwarfs are excellent targets for observation in the optical regime due to the contrast of 'white light' emission with the luminosity of the quiescent photosphere (Walkowicz et al. 2011; Jackman et al. 2021).

Flare outbursts last from minutes to hours. *Kepler* LC observations will miss short duration events. We visually examined all SC data and found two flaring events with peak amplitudes at 973.8961 and 1337.5025 BKJD, shown in Fig. 8. The flare durations are 8.83 and 7.85 min, respectively. The first flare occurs approximately 2.5 d after the star-spot detected during the planet's 23rd transit, but we cannot confirm that the features are related.

To determine the energy released, E_f, we followed the methodology of Kővári et al. (2007). The flare energy is a multiple of stellar quiescent flux, described by

$$E_f = \epsilon_f F_\star, \tag{9}$$

where ϵ_f is the relative flare energy, and $F_\star$ is the stellar quiescent flux.

The relative flare energy is the integral of normalized flux over the flare duration.

$$\epsilon_f = \int_{t_1}^{t_2} \left(\frac{I_{0+t}(t)}{I_0} - 1 \right) dt, \tag{10}$$

where t_1 and t_2 are the start and end flare times, and $\frac{I_{0+t}(t)}{I_0}$ is the normalized flux at each point.

The quiescent stellar flux, $F_\star$, is obtained by integrating the product of the *Kepler* response function and the *Planck* blackbody function over the *Kepler* bandpass from 348 to 970 nm

$$F_\star = \int_{\lambda_1}^{\lambda_2} 4\pi R_\star^2 B(\lambda) S_{\mathrm{Kep}}(\lambda) d\lambda, \tag{11}$$

where λ_1 and λ_2 are the minimum and maximum bandpass wavelengths (348 to 970 nm, respectively), $R_\star$ is the stellar radius, $B(\lambda)$ is the *Planck* blackbody function, and $S_{\mathrm{Kep}}(\lambda)$ is the *Kepler* response function.

Considering $T_{\mathrm{eff}} = 4840\ ^{+140}_{-190}$ K, the luminosity of KOI-883's quiescent photosphere is $6.4^{+0.9}_{-1.1} \times 10^{31}$ erg s^{-1}. Integrating the normalized fluxes of the first flare from 973.8913 to 973.8974 BKJD and the second flare from 1337.5018 to 1337.5072 BKJD (shown by the red dashed lines in Fig. 8) yields relative flare energies of 546.1 and 479.8, respectively. Thus, equation (9) yields flare energies of $3.5^{+0.5}_{-0.6} \times 10^{34}$ and $3.1^{+0.5}_{-0.5} \times 10^{34}$ erg for the first and second flares, respectively. Only such energetic flares will be detectable in white light due to their brightness and limited contrast with the photosphere (Günther et al. 2020). Superflare energies can exceed those of a typical solar flare, which has an energy of the order of 10^{29}–10^{32} erg (Yang & Liu 2019).

4.5 Star-spot mapping

The observation of sunspots at different latitudes has shown that the Sun's rotation is greatest at the equator and decreases towards the poles. Solar-type differential rotation is predicted and observed in non-slowly rotating cool stars (Gastine 2013; Benomar et al. 2018). The methods by which stellar differential rotation has been assessed include star-spot tracking, DI, Fourier analysis of spectra and photometric data, and asteroseismology (see Oláh et al. 2009; Gastine 2013; Benomar et al. 2018; Rüdiger et al. 2019, and references therein).

High-precision light curves have presented the ability to track individual star-spots for the measurement of latitudinal rotation period (Silva-Valio 2008) and spin–orbit alignment (e.g. Tregloan-Reed, Southworth & Tappert 2013) as well as measure mean stellar rotation from flux modulation. By combining the rotation period at any transit latitude derivable from occulted star-spots with the mean stellar rotation period, a stellar rotation profile may be constructed (Silva-Valio & Lanza 2011). Here, construction of KOI-883's rotation profile assumes the estimation of differential rotation from the mean stellar and transit latitude rotation periods for well-aligned stellar spin and planetary orbit axes.

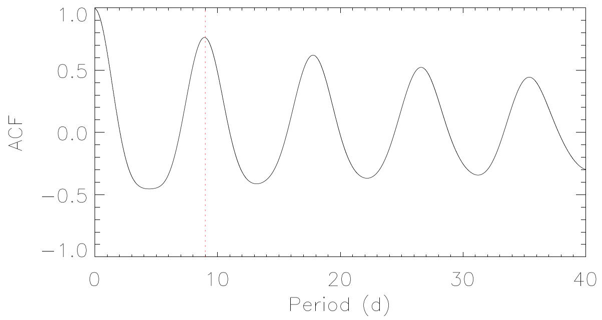

Figure 9. Autocorrelation function of the mean stellar rotation period. The dashed vertical line (red) crosses the first peak at 8.994 d.

The characteristics of star-spots resulting from transit fitting are assembled into a temporal map of the surface of KOI-883. In order to correctly place star-spots on the surface of KOI-883, the mean stellar rotation period must be computed since the observed longitudes are estimated in the stationary frame of the observer. The transited stellar face is continually refreshed by stellar rotation, causing the modulations in LC light curves as star-spot configuration changes. Lomb–Scargle analysis of the modulation yields a peak at 8.99 ± 0.03 d. McQuillan, Mazeh & Aigrain (2013) calculated a mean stellar rotation period of 9.015 ± 0.002 d via autocorrelation of LC data for Kepler quarters 3–14. Applying the same technique with the addition of data from quarters 15–17, a linear fit to the four peaks of the autocorrelation shown in Fig. 9 yields a mean stellar rotation period of 8.994 ± 0.016 d. Thus, 8.994 d is adopted as the mean stellar rotation period.

The stellar rotation period is used to translate star-spot longitudes in the observer's frame to longitudes in the frame that rotates with the star, as described by equation (12). Thus, star-spots are positioned along the 360° stellar circumference at the transit latitude.

$$lon_{\rm rot} = lon_s - 360^\circ \frac{n P_{\rm orb}}{P_\star}, \tag{12}$$

where n is the transit number, $P_{\rm orb}$ is the orbital period of the planet, and $P_\star$ is the mean stellar rotation period. Equation (4) was previously used to calculate projected longitudes on the stellar disc, lon_s, during star-spot modelling.

The map in Fig. 10 depicts the distribution of star-spots on the stellar surface with respect to *Kepler* observation time. Time 0 corresponds to the mid-transit time of the first transit in BKJD. Subsequent times reflect the 2.689 d orbital period of KOI-883b. Mapped spots are colour-scaled by intensity, the darkest and lightest spots having the greatest and least contrast with the photosphere, respectively. Their relative radii are also depicted by the size of the circles in the map.

Star-spot flux deficits have been calculated from intensity contrast with the photosphere and star-spot radii via equation (8). Integrated flux deficit with respect to stellar longitude is given in the bottom panel of Fig. 10. The peaks in flux deficit at -140° and 80° point to clusters of star-spots. Before 200 d, there is a cluster of star-spots between 50° and 100° lasting a minimum of 100 d. After 200 d, a cluster lasting 200 d appears in the opposite hemisphere from -160° to -120°. This infers active regions in the photosphere that change with time. The transit chord correlation method (TCC) of Dai et al. (2018) for the analysis of stellar magnetic activity and planet orbital obliquity also produced a plot of transit longitude versus time which shows 2 similar active regions. The TTC plot (Fig. 10; Dai et al. 2018) and our map in Fig. 10 do not consider a differentially rotating star. A spot map which takes in account the rotation period at the transit latitude will realign the spots thereby confirming or rejecting the possibility of active longitudes.

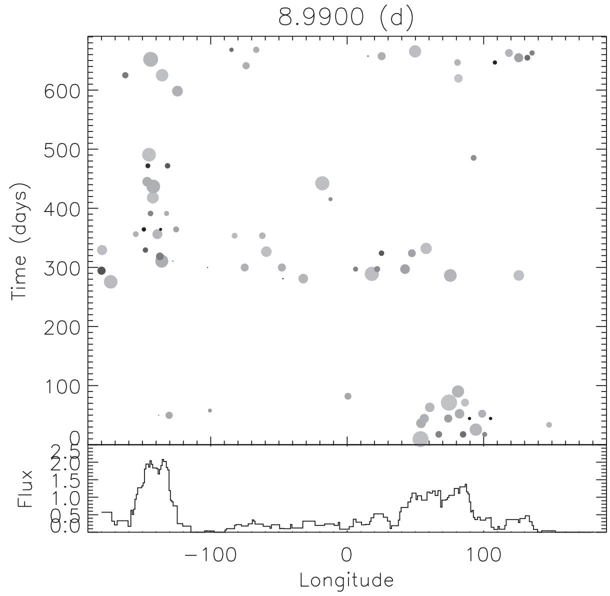

Figure 10. Top: Temporal spot map of the stellar surface at transit latitude -24.99° for the mean stellar rotation period. Star-spot intensity is represented in grey-scale, intensity increasing with depth of tone. Bottom: The total flux difference versus longitude.

4.6 Rotation period at the transit latitude

Autocorrelation of flux deficit has been successfully used to measure rotation rate at the transit latitude (Silva-Valio & Lanza 2011; Valio 2013; Valio et al. 2017; Zaleski et al. 2019, 2020; Netto & Valio 2020; Araújo & Valio 2021). For KOI-883, we consider the total flux deficit at each degree of longitude for the 78 fitted spots for different possible rotation periods. Varying the rotation period in steps of 0.01 d, we calculate the autocorrelation function of the spot flux deficit and estimate the FWHM of its main peak. The rotation period that resulted in the minimum FWHM is selected as the transit latitude rotation period.

As shown in Fig. 11, the minimum FWHM occurs for a rotation period of 8.59 ± 0.04 d at transit latitude -24.99°. Star-spot longitudes in the rotating stellar frame are recalculated using equation (12) by substituting the transit latitude rotation period for the mean stellar rotation period. The temporal map in Fig. 12 shows star-spot alignment when the latitudinal rotation period is considered. Indicative of a differentially rotating star, the notable active regions in Fig. 10 no longer appear.

Differential rotation is an important process of the solar dynamo responsible for the twisting of magnetic field flux tubes that become star-spots when they reach the photosphere. The Sun exhibits different rotation rates at different latitudes, with rotation fastest at the equator and decrementing towards the poles. Cool, active stars like the Sun are known to demonstrate solar-type differential rotation (Petit, Donati & Collier Cameron 2002; Reiners & Schmitt 2004).

The differential rotation of the Sun may be described by a simplified solar law, as follows,

$$\Omega(\alpha) = \Omega_{eq} - \Delta\Omega \ \sin^2(\alpha), \tag{13}$$

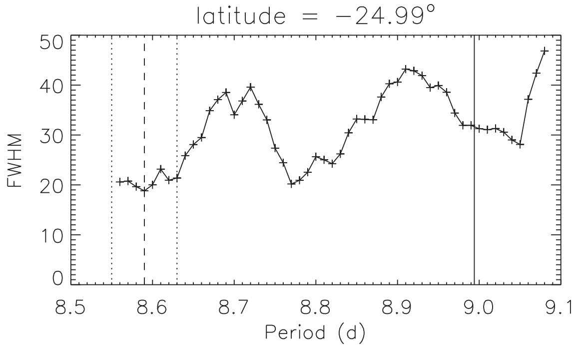

Figure 11. FWHM of flux deficit autocorrelation. The solid vertical line marks the average rotation period of 8.99 d, whereas the vertical dashed line marks the thinnest peak of the autocorrelation function at 8.59 d, the rotation period of the star at the transit latitude. The dotted vertical lines are the 0.04 d uncertainty in this period.

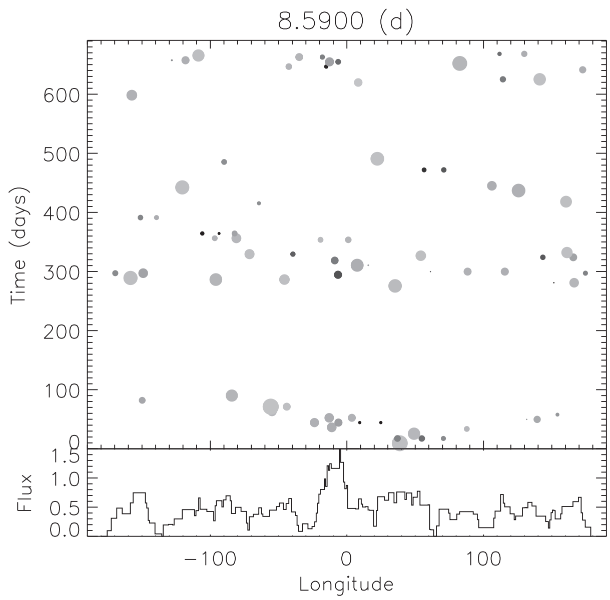

Figure 12. Top: Temporal spot map of the stellar surface for a rotation period of 8.59 d at transit latitude −24.99°. Star-spot intensity is represented in grey-scale, intensity increasing with depth of tone. Bottom: The total flux difference versus longitude.

where Ω is the angular velocity at stellar latitude α, Ω_{eq} is the equatorial angular velocity, and $\Delta\Omega$ is rotational shear, or the difference in angular velocity between the equator and pole.

Differential rotation can be measured if the mean stellar rotation rate and the rotation rate at any non-equatorial latitude is known. For extra-solar systems in which the host star is transited by a single exoplanet, star-spot mapping provides the rotation period at the projected stellar transit latitude (see previous section). Host star-single planet systems for which differential rotation has been calculated include CoRoT-2 (Silva-Valio & Lanza 2011), Kepler-17 (Valio et al. 2017), Kepler-63 (Netto & Valio 2020), Kepler-71 (Zaleski et al. 2019), and Kepler-45 (Zaleski et al. 2020), which are transited by a hot Jupiter. Differential rotation from rotation periods at three non-equatorial latitudes has been measured for Kepler-411, a K2 dwarf transited by 1 super-Earth and 2 mini-Neptune sized planets (Araújo & Valio 2021).

We estimate the differential rotation of KOI-883 by constructing a solar differential rotation profile given the transit latitude rotation period of 8.59 d. We assume a generic profile of the form

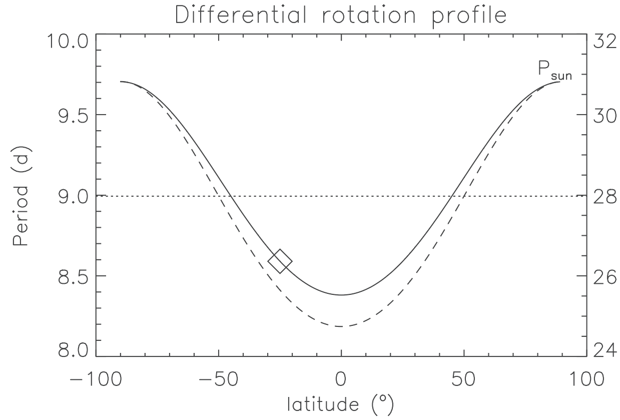

Figure 13. Differential rotation profiles of KOI-883 (solid line) and the Sun (dashed line) as a function of latitude. The diamond marks the 8.59 d rotation period of KOI-883 at transit latitude −24.99° estimated from transit mapping. The horizontal dotted line denotes the mean stellar rotation period of 8.994 d.

$$\Omega(\alpha) = A - B\ \sin^2\alpha, \tag{14}$$

where A and B are the stellar equatorial angular velocity and rotational shear, respectively.

To determine A and B, we solve a system of two equations by adding an expression for average rotation. The average rotation is the integral of equation (14) over the minimum and maximum latitudes at which star-spots emerge.

$$\bar{\Omega} = \frac{1}{(\alpha_2 - \alpha_1)} \int_{\alpha_1}^{\alpha_2} \left(A - B\ \sin^2\alpha\right) d\alpha, \tag{15}$$

where α_1 and α_2 are the minimum and maximum latitudes, respectively. If we first assume that star-spots can emanate close to the poles, integration over 0° to 90° yields lower limits for rotational shear and relative differential rotation, $\Delta\Omega = (0.102 \pm 0.011)$ rad d^{-1} and $\Delta\Omega/\bar{\Omega} = (14.6 \pm 1.5)$ per cent, respectively, where $\bar{\Omega} = 2\pi/P_\star$ and $P_\star$ is the mean stellar rotation period of 8.994 d. However, since KOI-883b is a rather large planet, the transit chord spans a latitude band 32° wide. Thus, if we consider that the spots may be located within ±16° in latitude from the mid-transit latitude of −25°, that is from −9° through −41°, then the limits for the rotational shear and relative differential rotation, are $\Delta\Omega = 0.069$–0.472 rad d^{-1} and $\Delta\Omega/\bar{\Omega} = 9.9$–$67.5$ per cent, respectively. In comparison, the generalized relation for rotational shear based on stellar effective temperature and rotation period published by Balona & Abedigamba (2016, equation 1) estimates $\Delta\Omega = 0.081^{+0.008}_{-0.013}$ rad d^{-1}. The value of $\Delta\Omega$ from Balona & Abedigamba (2016) relation is well within the interval of $\Delta\Omega$ found for KOI-883.

The differential rotation profile of KOI-883 given a mean stellar rotation period of 8.994 d and calculated transit latitude rotation period of 8.59 d is plotted in Fig. 13. The diamond marks transit latitude −24.99°. The solar rotation profile is shown by the dashed line with values given by the right axis for comparison.

5 SUMMARY AND DISCUSSION

We have presented the first retrieval of astrophysical parameters and estimates of solar dynamo activity for the early orange dwarf KOI-883 (0.7 M$_\odot$, 0.69 R$_\odot$) from individual star-spots and star-spot groups occulted in the equatorial region of the photosphere by a hot Jupiter companion. *Kepler* photometry of the faint star (*Kepler* magnitude

15.766) reveals both modulation due to the movement of star-spots in and out of the observer's view with stellar rotation and deep transits of Jupiter-sized exoplanet. Temporal maps of the stellar photosphere in the transit band constructed from modelled star-spot physical parameters reveal processes of a solar-type dynamo, i.e. a short-term activity cycle and solar-type differential rotation. Evidence of flaring, albeit rare, is also found in the light curves.

The transiting hot Jupiter KOI-883b (1.265 $R_{♃}$) orbits close to its host at a distance of 0.03 au in a plane whose inclination is approximately orthogonal to the stellar rotation axis. The planet's projection on the stellar face lies along a transit chord at -24.99° latitude. KOI-883b completes its orbit about the host dwarf star every 2.69 d. From a total of 254 possible transits, approximately 170 transits were observed by the *Kepler* telescope in SC mode. From these transits, we extracted 78 occulted star-spots whose signatures exceeded the rms noise of SC data.

The differences in age, mass, and rotation period between KOI-883 and the Sun highlight interesting comparisons of sunspot and star-spot physical attributes. Sunspots range in radial size from 7.5×10^2 to 2.5×10^4 km, with many the radius of Earth (6.24×10^3 km) and occasionally some the radius of Jupiter (7×10^5 km). Star-spots on KOI-883 are a factor of 10 larger than sunspots, ranging in size from 9.69×10^3 to 1.21×10^5 km, with a median size of 5.74×10^4 km. Following the age–rotation–activity relation of Barnes et al. (2005), the dynamo processes active in a less massive star that is much younger and rotating significantly faster than the Sun give rise to larger spots, or active regions.

The radial size of an exoplanet probing the stellar surface also affects observed star-spot size (Tregloan-Reed & Unda-Sanzana 2019). A Jupiter-sized planet will cover more area in a wider transit band than a smaller planet. The largest planet transiting the K2V star Kepler-411 is a mini-Neptune. The median size of occulted star-spots on Kepler-411 is approximately 1.5×10^4 km, with most less than 3.5×10^4 km and few sized 5.5×10^4 km (Araújo & Valio 2021). The median size of KOI-883's star-spots is roughly a factor of 4 larger. The largest spotted area on KOI-883 is twice as large as that on Kepler-411. If spot groups exist on the stellar surface, information from an occulting Jupiter-sized planet will provide a better measure of a group's radial extent, rather than individual spots.

The presence of large star-spots on KOI-883 does not guarantee flaring activity. It is believed that flaring stars have larger star-spots than non-flaring stars, though the connection between star-spot size and flare rate has yet to be confirmed. The majority of stars in the *Kepler* catalogue have large spots but do not flare (Yang & Liu 2019). Flaring shows clearer dependence on stellar rotation. The interplay of rotation and convection in the solar dynamo is believed to be responsible for the generation of magnetic field energy that is released as flares (see Günther et al. 2020, and references therein). From a sample of over 700 flaring *Kepler* stars, K and M dwarfs presented greatest flaring for rotation periods between approximately 10 and 35 d (Balona 2015). In comparison, F stars flared most often at rotation periods shorter than 10 d, and G stars also flared for short rotation periods with flaring decreasing for rotation period longer than 20 d.

We detected two flares with durations of 7.85 and 6.86 min and energies of 3.1×10^{34} and 2.7×10^{34} erg, respectively, separated by 1.1 yr. For K0V–K8V stars in the first data release from the Next Generation Transit Survey (NGTS DR1[4]), Jackman et al. (2021) found flares lasting 2–15 min with bolometric energies between 10^{32} and 10^{36} erg. The subset of K2V–K4V dwarfs had bolometric energies of the order of 10^{34}–10^{35} erg. They also projected that a flare with an energy of 10^{34} erg will occur on a K2V–K4V star every $1.7^{+2.1}_{-0.9}$ yr.

KOI-883's rotational shear presents a new data point for solar dynamo theory. Küker & Rüdiger (2011)'s models of the surface differential rotation for ZAMS stars having a rotation period of 2.5 d highlighted the dependence of shear on stellar effective temperature. For a temperature of 4800 K, surface differential rotation is approximately 0.05 rad d^{-1}. Kitchatinov & Olemsky (2012) arrived at a similar value. In their study of active *Kepler* stars, Reinhold et al. (2013) found that $\Delta\Omega$ gently trended upwards to 0.11 rad d^{-1} as stellar effective temperature increased from 3500 to 6000 K, inferring a weak dependence on temperature. Their weighted means of $\Delta\Omega$ for different temperature bins were all close to 0.07 rad d^{-1}. For $T_{\rm eff}$ = 4800 K, most stars had a shear value between 0.04 and 0.10 rad d^{-1}. Our value of $\Delta\Omega = 0.102$ rad d^{-1} is certainly plausible.

The mean stellar effective temperatures of KOI-883 and Kepler-411 differ by only a few degrees. Yet, the rotational shear of Kepler-411 is estimated to be only 0.050 rad d^{-1}. The reason for differing values of differential rotation may lie with the exoplanets and not the stars. The distinguishing feature between the two stellar systems is the planet configuration: KOI-883 is orbited by the hot Jupiter KOI-883b, and Kepler-411 is orbited by two mini-Neptunes (Kepler-411c and d) and one super-Earth (Kepler-411b). Kepler-411b orbits at a distance of 0.049 au, while the semimajor axes of Kepler-411c and d are 0.080 and 0.29 au. KOI-883b orbits closer to its host star at 0.039 au. A giant planet in close proximity of its host will have a greater effect on stellar dynamics than a small planet farther away (Cuntz, Saar & Musielak 2000). Hot Jupiters and their host stars can interact via their magnetospheres (see Cauley et al. 2018, and references therein) and magnetized winds (Strugarek 2016).

Magnetic star–planet interaction (MSPI) impacts dynamo processes responsible for magnetic activity and may alter magnetic topology (Shkolnik et al. 2009). Stellar flares and chromospheric variations may be evidence of MSPI, as indicated by observations of the primary star in a binary system, K dwarf HD189733 A, which is orbited by a hot Jupiter (Poppenhaeger 2015; Cauley et al. 2018). Nevertheless, while one can speculate that MSPI may be powerful enough for the planet to affect magnetized flows in the stellar convective zone, dynamo action and flare activity, modelling of possible MSPI for this system is beyond the scope of this paper.

In conclusion, KOI-883 is a notable combination of a low-mass, moderately active orange dwarf and a hot Jupiter whose transits enable star-spot mapping in some detail. A low-latitude region of individual or grouped star-spots provides evidence of a moderately high but expected rotational shear consistent with our understanding of stellar dynamo behaviour. The two observed energetic flares are similar to those observed for other magnetically active cool dwarfs.

ACKNOWLEDGEMENTS

We thank the anonymous referee for a diligent review with comments and suggestions that improved the content herein.

We also thank P. Wilson Cauley for sharing an IDL implementation of the Goodman & Weare MCMC.

AV acknowledges the São Paulo Research Foundation (FAPESP) (Grant #13/10559-5).

This paper includes data collected by the *Kepler* mission. Funding for the *Kepler* mission is provided by the National Aeronautics and Space Administration (NASA) Science Mission directorate. *Kepler* light-curve data were obtained from the NASA Exoplanet Archive,

[4]http://eso.org/rm/api/v1/public/releaseDescriptions/122

which provides public access to *Kepler* Mission data. The primary archive of all *Kepler* data is provided by the Barbara A. Mikulski Archive for Space Telescopes (MAST) at the Space Telescope Science Institute (STScI).

This work has also made use of data from the European Space Agency (ESA) mission *Gaia* (https://www.cosmos.esa.int/gaia), processed by the *Gaia* Data Processing and Analysis Consortium (DPAC; https://www.cosmos.esa.int/web/gaia/dpac/consortium). Funding for the DPAC has been provided by national institutions, in particular the institutions participating in the *Gaia* Multilateral Agreement.

DATA AVAILABILITY

The data underlying this article are available in the NASA Exoplanet Archive at https://exoplanetarchive.ipac.caltech.edu/ and in the Mikulski Archive for Space Telescopes (MAST) Portal at https://mast.stsci.edu/portal/Mashup/Clients/Mast/Portal.html, and can be accessed with target identification number 7380537, as listed in the *Kepler* Input Catalog. Stellar parameters are also available in the *Gaia* Early Data Release 3 Archive at ESA at https://gea.esac.esa.int/archive/, and can be accessed with target name KOI-883.

REFERENCES

Afram N., Berdyugina S. V., 2015, A&A, 576, A34
Aigrain S. et al., 2015, MNRAS, 450, 3211
Albrecht S. et al., 2012, ApJ, 757, 18
Alsubai K. A. et al., 2011, MNRAS, 417, 709
Anderson J. M., Korhonen K., 2015, MNRAS, 448, 3053
Angus R. et al., 2019, AJ, 158, 173
Araújo A., Valio A., 2021, ApJ, 907, L5
Balona L. A., 2015, MNRAS, 447, 2714
Balona L. A., Abedigamba O. P., 2016, MNRAS, 461, 497
Barnes J. R., Collier Cameron A., Donati J. -F., James D. J., Marsden S. C., Petit P., 2005, MNRAS, 357, L1
Batalha N. M. et al., 2013, ApJS, 204, 24
Beck J. G., 2000, Sol. Phys., 191, 47
Becker J. C., Vanderburg A., Adams F. C., Khain T., Bryan M., 2017, ApJ, 154, 230
Benomar O. et al., 2019, Science, 361, 1241
Berdyugina S. V., 2004, Sol. Phys., 224, 123
Berdyugina S. V., 2005, Living Rev. Sol. Phys., 2, 8
Biazzo K., Frasca A., Catalano S., Marilli E., Henry G. W., Taz G., 2002, Mem. Soc. Astron. Ital. Suppl., 2, 220
Bondar N. I., Katsova M. M., Livshits M. A., 2019, Geomagn. Aeronomy, 59, 832
Bonomo A. S., Lanza A. F., 2012, A&A, 547, A37
Borucki W. J., 2010, Science, 327, 977
Bourque M. et al., 2021, The ExoPlanet Characterization Toolkit (ExoTCK), 1.0.0, Zenodo, Available at:https://zenodo.org/record/4556063/export/hx#.YegNP_jhWUk
Brown D. J. A., 2014, MNRAS, 442, 1844
Brown S., Donati J. F., Rees D., Semel M., 1991, A&A, 250, 463
Bryan M. L. et al., 2012, ApJ, 750, 84
Carrington R. C., 1859, MNRAS, 20, 13
Carroll T. A., Strassmeier K. G., Rice J. B., Künstler A., 2012, A&A, 548, A95
Cauley P. W., Shkolnik E. L., Llama J., Bourrier V., Moutou C., 2018, ApJ, 156, 262
Claret A., 2000, A&A, 863, 1081
Claret A., Bloemen S., 2011, A&A, 529, A75
Claret A., Hauschildt P. H., Witte S., 2012, A&A, 546, A14
Clement E. P., 2014, Am. J. Math. Stat., 4, 214
Covas E., 2017, A&A, 605, A44
Cuntz M., Saar S. H., Musielak Z. E., 2000, ApJ, 533, L151
Dai F., Winn J. N., Berta-Thompson Z., Sanchis-Ojeda R., Albrecht S., 2018, ApJ, 155, 177
Dai F., Winn J. N., Yu L., Albrecht S., 2016, ApJ, 153, 40
Davenport J. R. A., 2016, AJ, 829, 23
Davenport J. R. A., Covey K. R., Clarke R. W., Boeck A. C., Cornet J., Hawley S. L., 2019, ApJ, 871, 241
Davenport J. R. A., Hebb L., Hawley S. L., 2015, ApJ, 806, 212
Dawson R. A., 2014, ApJ, 730, L31
Deng L. H., Zhang X. J., Li G. Y., Deng H., Wang F., 2019, MNRAS, 488, 111
Donati J. F. et al., 2008, MNRAS, 390, 545
Eggleton P. P., Kiseleva-Eggleton L., 2001, ApJ, 562, 1012
Estrela R., Valio A., 2016, in Nandi D., Valio A., Petit P., eds, Proc. of the IAU No. 328. Vol. 12, Cambridge University Press, Cambridge, UK, p. 152
Foreman-Mackey D., Hogg D., Lang D., Goodman J., 2013, PASP, 125, 306
Gaia Collaboration, 2016, A&A, 595, A1
Gaia Collaboration, 2021, A&A, 649, A1
Gastine T., Yadav R. K., Morin J., Reiners A., Wicht J., 2013, MNRAS, 438, L76
Gilliland R. L. et al., 2011, ApJS, 197, 6
Goodman J., Weare J., 2010, Commun. Appl. Math. Comput. Sci., 5, 68
Gordovskyy M., Lozitsky V. G., 2014, Sol. Phys., 289, 10
Grimes R., Pinter B., Morgan H., 2020, Sol. Phys., 295, 87
Günther M. N., Zhan Z., Seager S., Rimmer P. B., Ranjan S., 2020, AJ, 159, 60
Hamer J. H., Schlaufman K. C., 2019, AJ, 158, 190
Hathaway D. H., 2015, Living Rev. Sol. Phys., 12, 2
Hebrard G. et al., 2013, A&A, 549, A134
Hellier C. et al., 2012, MNRAS, 426, 739
Holczer T. et al., 2015, ApJ, 807, 170
Hubbard A., Rheinhardt M., Brandenburg A., 2011, A&A, 536, A48
Ilin E., Schmidt S. J., Davenport J. R. A., Strassmeier K. G., 2019, A&A, 622, A135
Isik E., Schmidtt D., Schussler L., 2011, A&A, 527, A135
Jackman J. A. G. et al., 2021, MNRAS, 504, 3246
Jeffries R. D., Jackson R. J., Briggs K. R., Evans P. A., Pye J. P., 2011, MNRAS, 411, 2099
Jenkins J. M. et al., 2010, ApJ, 173, L87
Joshi B., Veronig A., Manoharan P. K., Somov B. V., 2012, Astrophysics and Space Science Proceedings. Vol. 33, Springer, Verlag Berlin Heidelberg, p. 29
Kitchatinov L., Olemsky S., 2012, MNRAS, 423, 3344
Kővári Zs., Oláh K., Krisovics L., Vida K., Forgács-Dajka E., Strassmeier K. G., 2017, Astron. Nachr., 338, 903
Kővári Zs., Vilardell F., Ribas I., Vida K., van Driel-Gesztelyi L., Jordi C., Oláh K., 2007, Astron. Nachr., 328, 904
Kraft R. J., 2016, ApJ, 150, 551
Küker M., Rüdiger G., 2005, A&A, 422, 1023
Küker M., Rüdiger G., 2011, Astron. Nachr., 332, 933
Küker M., Rüdiger G., Oláh K., Strassmeier K. G., 2019, A&A, 622, A40
Li L. H., Sofia S., Belvedere G., 2005, AJ, 629, 1164
Mancini L. et al., 2014, MNRAS, 443, 2391
Mancini L. et al., 2017, MNRAS, 465, 843
Matt S. P., Do Cao O., Brown B. P., Brun A. S., 2011, Astron. Nachr., 332, 897
Maunder E. W., 1904, MNRAS, 64, 747
McQuillan A., Mazeh T., Aigrain S., 2013, ApJS, 775, L11
Mehrabi A., He H., Khosroshahi H., 2017, ApJ, 834, 207
Morris B., Hebb L., Davenport J. R. A., Rohn G., Hawley S. L., 2015, ApJ, 846, 99
Namekata K. et al., 2019, ApJ, 871, 187
Neilson H. R., McNeil J. I., Ignace R., Lester J. B., 2017, ApJ, 845, 65
Netto D. Y. S., Valio A., 2020, A&A, 635, 78
Nichols-Fleming F., Blackman E. G., 2020, MNRAS, 491, 2706
Nizamov B. A., Katsova M. M., Livshits M. A., 2017, Astron. Lett., 43, 202
Oláh K. et al., 2009, A&A, 501, 703

Oláh K., Kővári Sz., Petrovay K., Soon W., Baliunas S., Kollath Z., Vida K., 2016, A&A, 590, A133
Ortiz A., Solanki S. K., Domingo V., Fligge M., Sanahuja B., 2002, A&A, 388, 1036
Pan Y., Fu J.-N., Zong W., Zhang X., Wang J., Li C., 2002, ApJ, 905, 67
Petit P., Donati J.-F., Collier Cameron A., 2002, MNRAS, 334, 374
Pettersen B. R., 1989, Sol. Phys., 121, 299
Poppenhaeger K., 2015, in Garcia R. A., Ballot J., eds, CoRoT Symposium 3/Kepler KASC-7 Joint Meeting. Vol. 101, EPJ Web of Conf., Toulouse, France, p. 05002
Reiners A., 2012, Living Rev. Sol. Phys., 9, 1
Reiners A., Schmitt J. H. M. M., 2004, in Maeder A., Eenens P., eds, Proc. IAU Symp. 215, Stellar Rotation. Astron. Soc. Pac., San Francisco, p. 138
Reinhold T., Reiners A., Basri G., 2013, A&A, 560, A4
Riello M. et al., 2021, A&A, 649, A3
Rüdiger G., Küker M., Käpylä P. J., Strassmeier K. G., 2019, A&A, 630, A109
Savanov I. S., Dmitrienko E. S., Pandei D. S., Karmakar S., 2018, Astrophys.Bull., 73, 454
Schrijver C. J., Swaan C., 2000, Solar and Stellar Magnetic Activity. Cambridge Univ. Press, New York
Schüssler M., Caligari P., Ferriz-Mas A., Solanki S. K., Stix M., 1996, A&A, 314, 503
See V. et al., 2016, MNRAS, 462, 4442
Semel M., 1989, A&A, 225, 456
Shapiro A. I., Solanki S. K., Krivova N. A., Yeo K. L., Schmutz W. K., 2016, A&A, 589, A46
Shibata K., Megara T., 2012, Living Rev. Sol. Phys., 8, 6
Shkolnik E., et al., 2009, in Stempel St. A. S. E., ed. 15th Cambridge Workshop on Cool Stars, Stellar Systems and the Sun. Vol. 1094, AIP Conf. Proc., p. 275
Silva A. V. R., 2003, ApJ, 585, L147
Silva-Valio A., 2008, ApJ, 683, L179
Silva-Valio A., Lanza A. F., 2011, A&A, 529, 36
Silva-Valio A., Lanza A. F., Alonso R., Barge P., 2010, A&A, 510, 25
Sing D. K., 2010, A&A, 510, A21
Smith J. C. et al., 2012, PASP, 124, 919
Solanki S. K., 2002, Astron. Nachr., 323, 165
Strugarek A., 2016, ApJ, 833, 140
Stumpe M. C. et al., 2012, PASP, 124, 984
Suarez Macareno A., Rebolo R., Gonzalez Hernandez J. I., 2018, A&A, 595, A12
Szabo R., Szabo Gy. M., Dalya G., Simon A. E., Hodosan G., Kiss L. L., 2013, A&A, 553, A17
Thompson S. E. et al., 2016a, Kepler Data Release 25 Notes (KSCI-19065-002)
Thompson S., Fraquelli D., Van Cleve J., Caldwell D., 2016b, Kepler Science Document KSCI-10008-006
Toriumi S., Airapetian V. S., Hudson H. S., Schrijver C. J., Cheung M. C. M., DeRosa M. L., 2020, ApJ, 902, 36
Tregloan-Reed J. et al., 2015, MNRAS, 450, 1760
Tregloan-Reed J., Southworth J., Tappert C., 2013, MNRAS, 428, 3671
Tregloan-Reed J., Unda-Sanzana E., 2019, A&A, 630, A114
Tregloan-Reed J., Unda-Sanzana E., 2021, A&A, 649, A130
Valio A., 2013, in Chavez M., Bertone E., Vega O., De la Luz V., eds, ASP Conf. Ser. Vol. 472, New Quests in Stellar Astrophysics III: A Panchromatic View of Solar-Like Stars, With and Without Planets. Astron. Soc. Pac., San Francisco, p. 239
Valio A., Estrela R., Netto Y., Bravo J. P., de Medeiros J. R., 2017, ApJ, 835, 2
Vogt S. S., Penrod G. D., 1983, in Rodono M., Byrne P., eds, IAU Colloquium. Vol. 71, Reidel, Dordrecht, p. 379
Walkowicz L. M. et al., 2011, ApJ, 141, 50
Winn J. N., Fabrycky D., Albrecht S., Johnson J. A., 2010, ApJ, 718, L145
Yadav R. K., Gastine T., Christensen U. R., Reiners A., 2013, A&A, 573, A68
Yan X. L., Wang J. C., Kong D. F., 2008, MNRAS, 391, 1887
Yang H., Liu J., 2019, ApJS, 241, 29
Zaleski S. M., Valio A., Carter B. D., Marsden S. C., 2020, MNRAS, 573, A68
Zaleski S. M., Valio A., Marsden S. C., Carter B. D., 2019, MNRAS, 484, 618

This paper has been typeset from a TEX/LATEX file prepared by the author.